



# **Symmetry Enforced, *a priori* RF Shimming in MRI for the Human Head at High Field Strengths**

**Jörg Felder<sup>1</sup>, N. Jon Shah<sup>1,2</sup>**

<sup>1</sup>Forschungszentrum Jülich GmbH, Institute of Neuroscience and Medicine – 4, Jülich, Germany

<sup>2</sup>RWTH Aachen University, Faculty of Medicine, Department of Neurology, JARA, Aachen, Germany

**ABSTRACT:** To obtain an *a priori* RF shim set for in vivo measurements of the human head where derivation and implementation are feasible on standard MRI systems without the need for sophisticated hard- or software. The method is targeted for initial anatomical scout scans and adjustments on high field scanners. Tailoring a rotationally symmetric phantom to be electrically large will produce characteristic interference patterns. This pattern is employed to enforce rotational symmetry in MRI images acquired with a multi-element transmit coil by adjusting transmit phases and/or amplitudes. Using the *a priori* shim on a human head defocuses the transmit fields, resulting in images with reduced signal dropouts. Three different sized adult heads were scanned with the predetermined shim set and a coil array consisting of eight transceiver elements. The images were found to show better image homogeneity than CP mode excitation and performed only slightly worse compared to a per subject RF shim. Relatively homogeneous excitation can be achieved with a pre-determined RF shim set. The homogeneity is sufficient for static field shimming and scout imaging. Primary application is the development of double resonant head coils with a fixed RF shim set for the proton channel intended for high field imaging in systems that do not possess parallel transmission capabilities.

**KEYWORDS:** Magnetic resonance imaging, MRI, B<sub>1</sub> shimming, predetermined shim, electromagnetic interference, human head, high field, parallel transmission.

## **I. INTRODUCTION**

At high field strength, 7T and above, circular polarization of transmit fields can result in parts of the acquired image showing different contrast or no signal at all due to destructive interference (1). Examples are shown in Figure 1 for two healthy volunteers. As a relatively simple method to achieve homogeneous excitation at high field strength, RF shimming has been introduced. A multitude of strategies to obtain suitable shim sets have been invented - see for example (2-5). Most of these require the acquisition of B<sub>1</sub><sup>+</sup> field maps and the calculation of a per subject shim set. While this is an approach that potentially yields optimum transmit field homogeneity, per subject shimming is only practical when the MR scanner is equipped with parallel transmit channels since changing the relative phase of transmit elements by inserting cables of appropriate length is a very tedious endeavour. Furthermore, it requires an additional acquisition and prolongs measurement time.

A possible solution to obtaining an *a priori* shim set might be to measure a number of subjects, carry out RF shimming on these and average the obtained results. However, since B<sub>1</sub> distribution is not a linear function of transmitter phases but rather contains a number of local solutions of almost identical homogeneity (6), averaging might not result in a usable shim set and additionally requires scanning multiple subjects for each novel coil array. The approach described here is based on an observation, which, to the best of the authors' knowledge, was first described, by Collins and co-workers (7). A coil with elliptical cross section was reported to cause the central brightening artefact to become less distinct than in a setup with rotational symmetry. This indicates that the distinctiveness of B<sub>1</sub><sup>+</sup> cancellation is reduced with an elliptical geometry, which could potentially reduce transmit field inhomogeneity.

# International Journal of Advanced Research in Electrical, Electronics and Instrumentation Engineering

(An ISO 3297: 2007 Certified Organization)

Vol. 5, Issue 1, January 2016

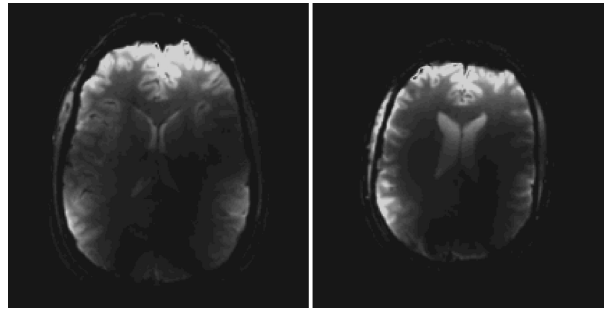


Figure 1: GRE images obtained on two volunteers when driving transmit elements with 45° phase offsets.

Based upon this observation we present the reverse approach. It employs an image-based RF shimming algorithm that enforces circular polarization (CP) on images acquired from a cylindrical phantom with the characteristic central brightening surrounded by a ring of destructive interference. When imaging the human brain, which has an elliptical cross section, this shim setting reduces the distinctiveness of destructive interferences.

The advantage of a predetermined RF shim set is that it can directly be used for *in vivo* (scout) imaging or to run adjustments like  $B_0$  shimming for X-nucleus experiments in systems without parallel transmit capabilities. On scanners with multiple transmitters, the method may be used as a sound starting point to carry out subject-specific RF shimming. Here it can also aid in  $B_1$  mapping since many sequences require initial shim sets for reliable measurements (8). Notwithstanding the previous statement, there are also methods that work independent of an initial shim (9).

Special emphasis has been put on the most convenient implementation of the algorithm so that it can be implemented on standard MR systems. The method described here can be used without the need for a dedicated  $B_1$  mapping sequence – given that the sum-of-squares receive profile is sufficiently homogeneous. In addition, the fixed phase relation of an *a priori* shim set allows easy specific absorption rate (SAR) handling. SAR can be obtained from EM simulations of the human head using the predetermined fixed phase relation and transmit power can be limited accordingly. In this case there is no need to compute complete Q-matrices and virtual observation points (10) or carry out worst-case approximations as is required for per patient shim sets or full parallel transmission.

## II. THEORY AND METHODS

### *Definition of circular polarization*

CP mode of operation is desirable as it is the eigenmode with the highest  $B_1$  efficiency in an unloaded resonator (11). It was thus chosen as the starting point for the shim method described here. However, while circular polarization is well defined for low frequency operation where a volume coil driven in quadrature produces a rotating transmit  $B_1^+$  field throughout the imaging volume, the definition and physical realization of CP mode operation becomes difficult in high field imaging. Due to the shorter wavelength, the  $B_1^+$  field cannot be circular polarized over the complete imaging volume. Possible definitions of CP mode operation might thus be a circular polarized  $B_1^+$  field at a given position in the volume (e.g. the centre) (1), minimum deviation from circular polarization within a given region-of-interest, or the driving of all transmit elements with phases according to their geometric rotation around the magnet axis. While the first two definitions are subject-specific, driving elements with phases according to geometrical rotation results in the characteristic intensity distribution with central brightening and signal dropouts in both temporal lobes (7) *in vivo*.

In the special case of rotational symmetry for both the phantom and the transmit array, however, all of the above definitions for CP mode become identical when the target region is chosen on the symmetry axis. However, in order to account for imperfections (such as cable length, phase of T/R switches, etc.) we employed an image-based method using regions of interest (ROIs) in the following derivation.

### *Shimming algorithm*

The idea of the proposed shimming algorithm is based on two observations. First, in *in vivo* head measurements at high field we observe similar excitation patterns independent of head size when the transmit coil is driven in CP mode, calibrated using a per subject method. Second, (7) reports less distinct signal cancellation when going from an elliptical

# International Journal of Advanced Research in Electrical, Electronics and Instrumentation Engineering

(An ISO 3297: 2007 Certified Organization)

Vol. 5, Issue 1, January 2016

to spherical symmetry. Employing the reverse direction by enforcing a symmetric excitation on a spherical cylindrical phantom, the “smearing” of transmit fields in the more elliptical geometry of the human head is expected to reduce local signal cancellation. In addition, since the signal cancellation patterns encountered in CP mode operation *in vivo* are similar, one time calibration of transmit phases on a symmetric phantom may be applicable to a wide range of head sizes.

The interference pattern of a spherical cylindrical phantom with a suitably shortened wavelength displays three distinct regions as shown in Figure 2 (a) and reported in (12) when the transmit field is circular polarized. The pattern has been calculated for a 9.4 T transceiver array consisting of eight unshielded loops with capacitive decoupling between its next neighbours (13). It is shown in Figure 2 (c). The EM simulations have been carried out with Microwave Studio (CST AG, Darmstadt, Germany). The phantom is a cylindrical water phantom (160 mm diameter and 370 mm long), which is doped with 1.24 g NiSO<sub>4</sub> and 2.62 g NaCl per 1000 g of H<sub>2</sub>O. The phantom has a permittivity of  $\epsilon_r = 78$  and a conductivity of 0.57 S/m as measured with a dielectric assessment kit (SPEAG, Zurich, Switzerland) at 400 MHz.

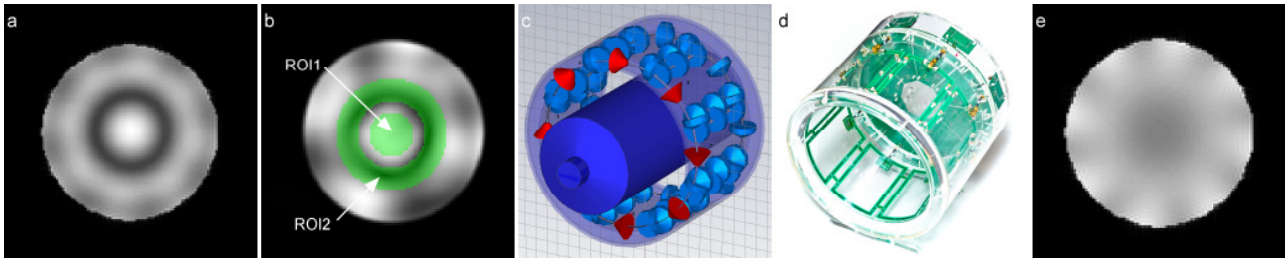


**Figure 2:** (a) circular polarized transmit magnetic field magnitude imposed on water phantom; (b) mask used to separate regions of interest – ROI1, ROI2, ROI3 are all pixels above threshold outside the ring ROI2; (c) EM simulation model of eight loop transceiver coil including the loading phantom; (d) realized coil array and (e) sum-of-squares recombined receive profile.

In order to calibrate the transmit field of a given parallel transmit array, we propose to use a cost function  $C$  in combination with small tip angle GRE images acquired for each transmit element individually and received with each receive element using phase sensitive (complex) signal acquisition. Doing so allows the received data to be treated as relative  $B_1^+$  maps – given that the recombination process is sufficiently homogeneous – and avoids the need for implementation of a  $B_1^+$  mapping sequence. Using EM simulations and the sum-of-squares recombination of receiver channels, the receive profile shown in Figure 2 (e) was obtained for the eight loop array.

The combined images can be subdivided using a mask as shown in Figure 2 (b) into three regions-of-interest: the central bright area (ROI1), the surrounding dark ring (ROI2) and the remaining pixels (ROI3). The quality of the individual shim set was evaluated using  $C$ , defined as

$$C(\mathbf{a}, \boldsymbol{\varphi}) = \lambda_1 \frac{\text{std}(\text{ROI1})}{\text{mean}(\text{ROI1})} + \lambda_2 \frac{\text{mean}(\text{ROI2})}{\text{mean}(\text{ROI1})} + \lambda_3 \frac{\text{max}(\text{ROI3})}{\text{mean}(\text{ROI1})} \quad (1)$$

where  $\text{std}()$ ,  $\text{mean}()$  and  $\text{max}()$  signify the standard deviation, mean and maximum signal intensities, respectively and  $\mathbf{a}$ ,  $\boldsymbol{\varphi}$  are the vectors containing drive amplitude and phase for each transmit channel. Note that similar measures are known from previous works, e.g. (14). The three terms in Eqn. (1) homogenize the central bright area, enforce the dark ring by minimizing its contribution and suppress regions with high signal intensities, respectively. The weighting factors  $\lambda_{1,3}$  were set to 1.00, 0.25 and 0.05, chosen to give similar contributions from all three regions. A slight modification of Eqn. (1) where  $\lambda_3$  was set to zero produces similar shim sets but in some cases resulted in hyperintensity at the periphery of the imaged phantom. Alternative choices of weighting factors  $\lambda_{1,3}$  are possible but the authors found the optimization to perform best when all three terms in equation (1) contribute about equal to the overall cost. However, this choice is empirical and purely based on the experience gained during the shimming experiments. Minimization of  $C$  was carried out using the “fminsearch” algorithm in Matlab (The Mathworks, Inc., Massachusetts, USA) and initial phases were set according to geometric rotation of the individual transmit elements, e.g. 45° phase increments between neighbouring channels for the eight loop array shown above.

### Experimental validation



# International Journal of Advanced Research in Electrical, Electronics and Instrumentation Engineering

(An ISO 3297: 2007 Certified Organization)

Vol. 5, Issue 1, January 2016

Measurements were carried out on a 9.4 T scanner (Siemens AG, Erlangen, Germany) with an eight-loop transceiver array constructed according to the simulation model. The coil was loaded with the appropriate phantom and GRE (TE=10ms/TR=100ms) images were acquired when transmitting with each element individually. The complex raw data was superimposed with the appropriate transmit phase to obtain the excitation pattern and a sum-of-squares reconstruction carried out to calculate a single image (15).

Starting with 45°, symmetry enforced shimming was carried out using the mask shown in Figure 2 (b). The extent of the ROIs was derived from the initial image – for the 256x256 matrix size used here the central ROI had a radius of 10 pixels and the ring structure was evaluated between the radii of 15 and 25 pixels. ROI3 encompasses the pixels not belonging to either ROI1 or ROI2. For the sake of simplicity and rotation symmetry along the z-axis, a single slice at the centre of the coil was chosen for the shim optimization.

To evaluate the obtained shim set for *in vivo* measurements, scans were performed on three healthy volunteers after having obtained written consent and within the framework of the clinical trial of our 9.4 T MR system approved by the local ethics committee (Ethik Kommission der RWTH Aachen, Pauwelsstraße 30, 52074 Aachen) and the Federal Institute of Drugs and Medical Devices. The volunteer images obtained were post-processed with a bias field correction algorithm (16). This allows one to remove any remaining signal inhomogeneity but also to visually assess the remaining regions with low excitation field – either by observing signal cancellation or regions with a decrease in local signal-to-noise ratio (SNR). For this purpose we employed the method proposed in (17) and implemented in the ITK software suite (available from <http://www.itk.org>) to evaluate the effect that post-processing benefits had on the shimmed *in vivo* images.

Investigation of *a priori* shimming as compared to shimming per volunteer was carried out by computing the “no voids” shim for each of the three volunteers in this study. This is obtained by setting the cost function to  $1/\min(SI)$  where SI is the signal intensity of all voxels in the region-of-interest, e.g. the head. Minimization of this cost function strongly penalizes any destructive interference in the excitation field as has been demonstrated in (3). The “no voids” shim was determined using simulated annealing as implemented in Matlab’s “simulannealbnd” function and a starting temperature (1e6 degrees) roughly half the magnitude of the inverse of the initial minimum pixel intensity. This starting temperature results in an initial step width large enough to cover the complete search space. For a fair comparison, “no void” shimming was carried out on the same image slice that has been used to derive the *a priori* shim set.

Despite the fact that SAR supervision for an *a priori* shim can take knowledge of the transmit phases into account, maximum transmit power for the *in vivo* measurements has been restricted using a worst case approximation. This approximation assumes constructive interference of electrical fields in all locations. It has been derived from EM simulations of the coil array using two different head voxel models (18). This was done because other RF shimming methods were investigated for comparison so that the transmit phase was unknown prior to shim optimization. However, since we used low flip angle sequences with long repetition times, power constraints were not an issue for any of the measurements shown here.

### III. RESULTS

Figure 3 (a) shows the image obtained when driving the coil with 45° increments between neighbouring elements. For this, the transmit phases were calibrated at the coil feeder panel (CFP) – the transmit coil connector. Clearly the expected symmetry is not present despite the fact that feeding cable length, T/R switches and coil elements respectively were constructed to have equal transmit phases. This indicates that the transmit field phases deviate from the driving phases through coil loading and remaining differences in electrical length between the individual coil elements as discussed above.

# International Journal of Advanced Research in Electrical, Electronics and Instrumentation Engineering

(An ISO 3297: 2007 Certified Organization)

Vol. 5, Issue 1, January 2016

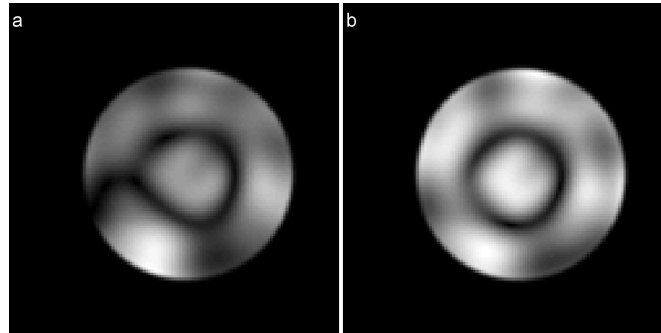


Figure 3: (a) gradient echo image (TE/TR= 10 ms/100 ms) acquired with the transmit channels calibrated to CP mode, (b) gradient echo image acquired after carrying out symmetry enforced  $B_1$  shimming.

The phantom image acquired after carrying out symmetry enforced shimming is shown in Figure 3 (b). The expected symmetry has been restored and the three regions can clearly be distinguished. In addition, the last term in Eqn. (1) successfully removed the region of hyperintensity encountered in the initial image. The transmit phases obtained from the shimming algorithm are listed in Table 1.

Table 1: Relative transmit phase settings for the individual RF shims employed. Here “CP” is used to denote 45 degree phase offsets between neighbouring elements, “a priori shim” refers to the suggested symmetry enforced shim set, and “no voids” indicates optimization using the 1/min cost function. All phases were referenced to channel #8 which served as master in the experiments.

Element	#8	#1	#2	#3	#4	#5	#6	#7
CP	0.0	45.0	90.0	135.0	180.0	225.0	270.0	315.0
A priori Shim	0.0	139.9	162.1	212.2	237.5	287.3	308.4	359.2
no voids, vol. #1	0.0	94.7	152.2	176.8	215.3	246.2	308.1	320.2
no voids, vol. #2	0.0	83.3	176.5	251.2	256.0	2.5	92.3	91.1
no voids, vol. #3	0.0	100.7	166.9	223.7	207.6	259.0	344.3	21.3

The images obtained *in vivo* from transverse gradient echo scans using the predetermined shim set are shown in Figure 4. It can be seen that the signal dropouts in the temporal lobes as well as central brightening can be removed. However, destructive interference cannot be avoided in all cases. Figure 4 (b) shows a region with almost no excitation and Figure 4 (a) has a region with low SNR just posterior of the brain stem which indicates low flip angles at this location.

A per volunteer comparison of GRE images using a priori shimming and subject specific shimming with the “no voids” cost function is given in Figure 5. While in the first volunteer some degree of signal cancellation remains prevalent independent of the shimming approach, the two other sets show a higher degree of homogeneity. As expected, in both cases the subject specific optimization produces better excitation homogeneity. However, the images acquired with the a priori shim set are sufficiently homogeneous for scouting and adjustments.

A qualitative comparison has been carried out by computing the standard deviation of image intensity after normalizing and threshold-based masking. The data is listed in Figure 5 at the bottom of each image showing that the standard deviation of signal intensity is comparable between a priori shimming and a subject specific (“no voids”) approach. Note that the standard deviation of image intensity contains image contrast when applied to GRE images and thus is only comparable per column in Figure 5.

# International Journal of Advanced Research in Electrical, Electronics and Instrumentation Engineering

(An ISO 3297: 2007 Certified Organization)

Vol. 5, Issue 1, January 2016

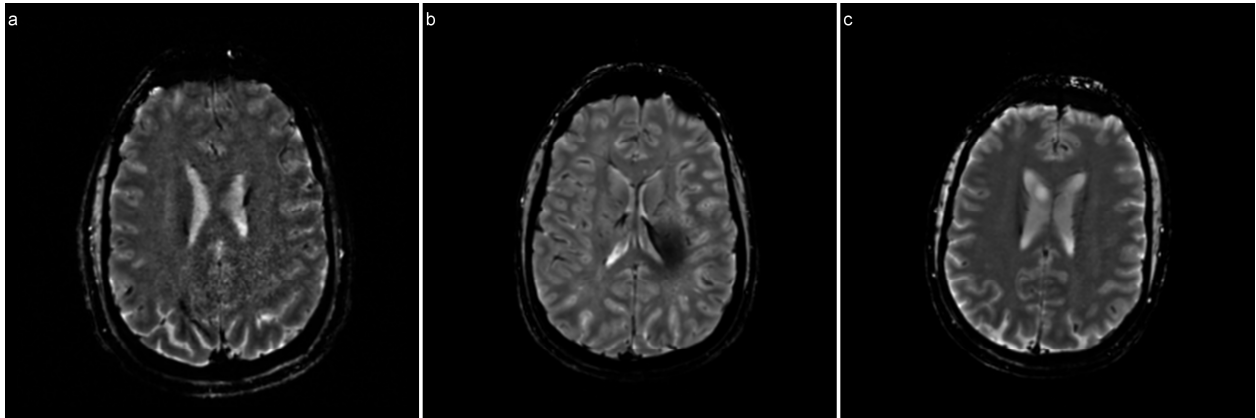


Figure 4: (a-c) images acquired from three healthy volunteers using the à priori shim set obtained from phantom measurements after bias field correction (Optimization passes (1<sup>st</sup>/2<sup>nd</sup>/3<sup>rd</sup> stage) = 250/125/125, spline distance = 50 pixels, spline order = 3, number of bins = 256).

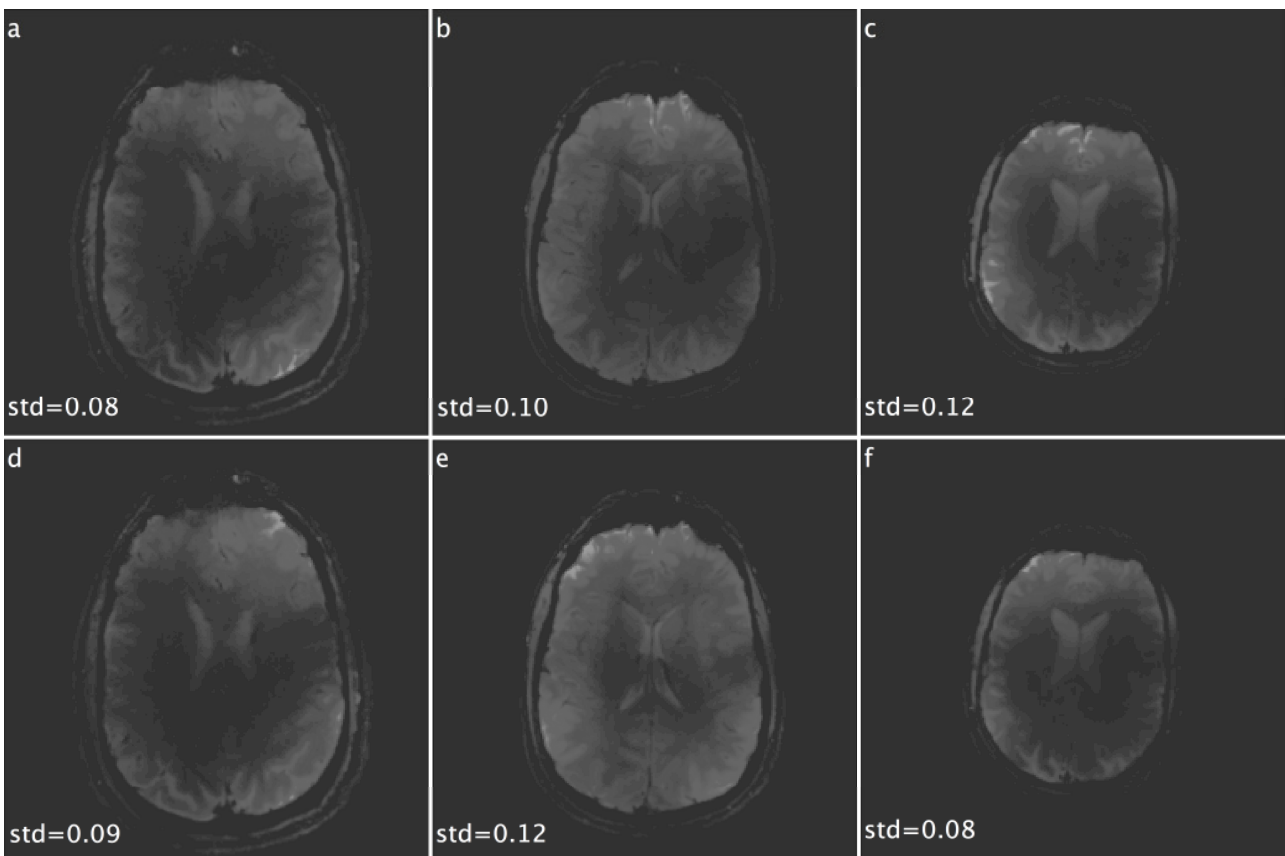
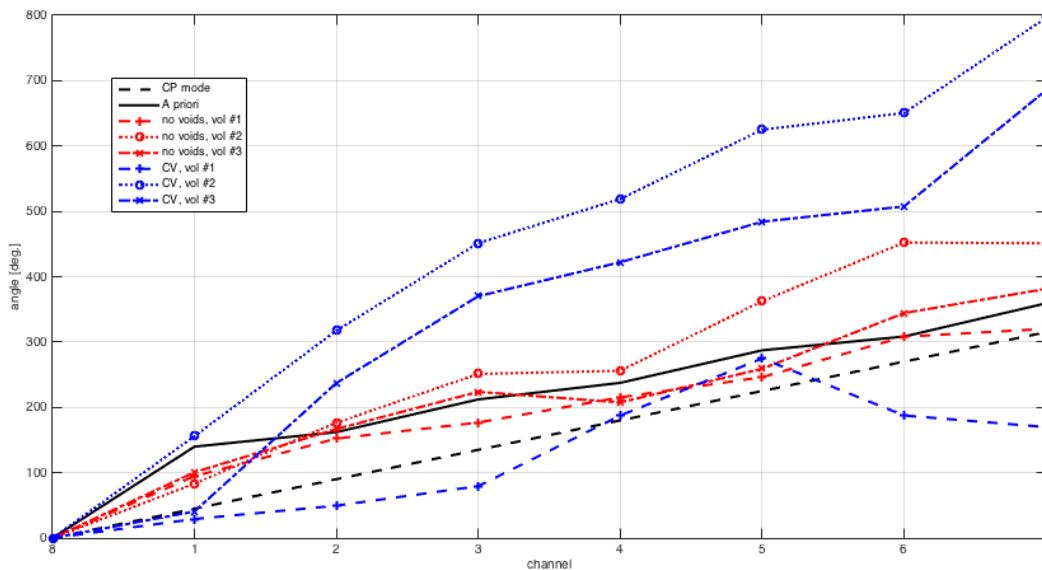


Figure 5: GRE images acquired from the three volunteers. The top row (a-c) is acquired with the single shim set obtained a priori by enforcing symmetry while the bottom row (d-f) shows the results obtaining the 1/min cost function (“no holes”) on a per subject basis. The numbers given are standard deviation after normalization of image intensity to unity mean.

A comparison of the different shimming approaches has been carried out by plotting the transmitter phases, see Figure 6. For the sake of clarity the phases have been unwrapped for all cases where phase jumps greater than 180° occurred

between neighbouring channels and referenced to the master channel (channel #8) for each shim set. Similar to the results reported in (7), the optimized phases appear to increase in a nearly linear fashion with channel number albeit sometimes showing an excursion of greater than  $360^\circ$ .



**Figure 6: Transmitter phases for the different  $B_1^+$  shims. Phase jumps greater than  $180^\circ$  have been unwrapped for clarity of presentation. For comparison circular polarization obtained from a centred ROI – and labelled “CV” – has been included. The line labelled CP mode refers to the case where  $45^\circ$  phase increments have been used to drive neighbouring channels.**

For the symmetry-enforced shim we observe roughly  $140^\circ$  phase difference between channel 8 and 1 while the remaining line in the phase plot continues almost parallel to the CP mode operation. The three “no voids” solutions are clustered around the line for symmetry enforced shimming – with the “no voids” shim for the third volunteer showing the highest deviation. This indicates that the symmetry-enforced shim set might present something like an average shim for the three volunteers measured despite a large variation in head size. Finally, we included circular polarization as obtained using a central region of interest in the *in vivo* measurements and driving the transmitters to achieve rotating polarization within the ROI. These curves are labelled “CV” in Figure 6. The slope of two of the CV shim sets is nearly twice that of the CP mode setting so that the current in the coils almost passes through two phase cycles. Again a similar finding was reported in (7).

A preliminary evaluation of whole brain performance of the *a priori* shimming method was carried out for two subjects by acquiring DREAM (9,19) ( $TE_{ste} = 2.22$  ms,  $TE_{fid} = 4.44$  ms,  $TR = 7.5$  s, 4 mm x 4 mm voxel size, 4 mm slice thickness) low resolution flip angle maps on multiple slices. The results are displayed in Figure 7. It can be seen that excitation homogeneity is achieved prevalently in the central slices, a result that was expected, since (3,20) reported that stacked elements in z direction are necessary to achieve homogeneous whole brain excitation. This was also confirmed by the introduction of “row delay” in (21).

## IV. DISCUSSION

Although many subject-specific shimming algorithms have been proven to work at 9.4 T, the results presented above are encouraging as they allow the construction of RF coils with predetermined phase relations between elements. Despite the fact that the hardware and software to carry out subject specific shimming is available, a predetermined shim set is a desirable feature for systems not equipped with multiple transmitter channels. As an example, the authors plan to implement a fixed shim set for proton scout imaging and  $B_0$  shimming together with X-nucleus coils, since the available parallel transmit system currently cannot be operated in combination with the X-nucleus transmitter.

# International Journal of Advanced Research in Electrical, Electronics and Instrumentation Engineering

(An ISO 3297: 2007 Certified Organization)

Vol. 5, Issue 1, January 2016

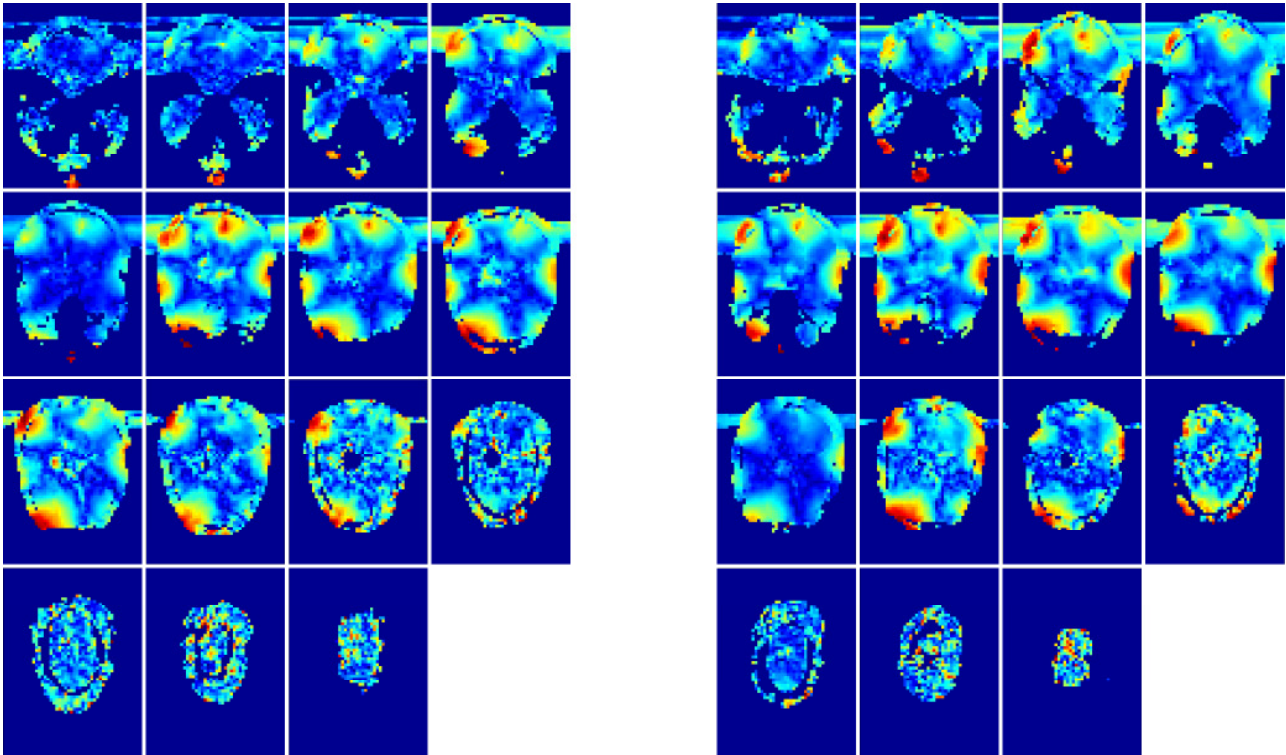


Figure 7: DREAM flip angle maps for two volunteers acquired with the phase encoding scheme.

It should be noted that the “no void” shim usually results in reduced average  $B_1^+$  amplitude and a slightly elevated specific absorption rate (SAR) as compared to CP mode (3). Since the phase set for the symmetry-enforced shim described here is similar to the ones obtained for the “no voids” solution, similar  $B_1^+$  field strength and SAR properties are to be expected. However, because of the inter-subject variability of SAR (6) this can only be seen as a rough performance indication. In this work, SAR was computed using a worst-case estimation and these SAR settings allowed for scouting and adjustments so that the intended applications using a fixed shim set are realizable.

Furthermore, in this treatment, combined amplitude and phase shimming has been neglected for the more readily accomplished variant of phase-only shimming, as this can be more easily implemented physically by adjusting the cable lengths on each coil element. In addition, full amplitude and phase control results in similar  $B_1^+$  patterns with only slight improvements in minimum field values (3).

Further investigation is required to assess the feasibility of *a priori* shimming for pathological changes where the field distribution can be expected to deviate from that of healthy anatomy. The investigation of other anatomical regions, e.g. the torso, is another interesting case. Since the torso is significantly larger than the human head, more complex signal cancellation patterns are to be expected. Even at 7 T, where the wavelength is a factor of approximately 1.35 longer than at 9.4 T, whole body imaging is challenging (22). Here a similar approach to the one presented above would at least require the addition of more transmit elements to obtain more degrees of freedom for the optimization. More probable, however, is that a predetermined set of phases will not give satisfactory results in a significant number of cases.

## V. CONCLUSION

In conclusion, relatively homogeneous excitation in the human head can be achieved at high field strength with a predetermined RF shim set as demonstrated here on three healthy volunteers at 9.4 T. This is useful in multiple ways,



# International Journal of Advanced Research in Electrical, Electronics and Instrumentation Engineering

(An ISO 3297: 2007 Certified Organization)

Vol. 5, Issue 1, January 2016

especially in systems without parallel transmit capabilities, but also for fast scout images without the need for field mapping or an elaborate workflow.

## VI. ACKNOWLEDGEMENT

The authors thank the hardware team of the Neuroscience Research Institute, Incheon, South Korea for support in constructing the coil array and acknowledge funding by the German Federal Ministry of Education and Research under grant number 13N9121. A. W. Magill, D. Tse and D. Brenner are acknowledged for helpful discussions and implementation of sequences.

NJS is funded in part by the Helmholtz Alliance ICAMED - Imaging and Curing Environmental Metabolic Diseases, through the Initiative and Network Fund of the Helmholtz Association. Further, NJS is supported by TRIMAGE, an EU FP7 project (Grant Agreement N° 602621).

## REFERENCES

1. Van De Moortele PF, Akgun C, Adriany G, Moeller S, Ritter J, Collins CM, Smith MB, Vaughan JT, Ugurbil K. B1 destructive interferences and spatial phase patterns at 7 T with a head transceiver array coil. *Magn Reson Med* 2005;54(6):1503-1518.
2. Curtis AT, Gilbert KM, Klassen LM, Gati JS, Menon RS. Slice-by-slice B1+ shimming at 7 T. *Magn Reson Med* 2012;68(4):1109-1116.
3. Hoffmann J, Shajan G, Scheffler K, Pohmann R. Numerical and experimental evaluation of RF shimming in the human brain at 9.4 T using a dual-row transmit array. *Magma* 2014;27(5):373-386.
4. Mao W, Smith MB, Collins CM. Exploring the limits of RF shimming for high-field MRI of the human head. *Magn Reson Med* 2006;56(4):918-922.
5. Shajan G, Kozlov M, Hoffmann J, Turner R, Scheffler K, Pohmann R. A 16-channel dual-row transmit array in combination with a 31-element receive array for human brain imaging at 9.4 T. *Magn Reson Med* 2014;71(2):870-879.
6. de Greef M, Ipek O, Raaijmakers AJ, Crezee J, van den Berg CA. Specific absorption rate intersubject variability in 7T parallel transmit MRI of the head. *Magn Reson Med* 2013;69(5):1476-1485.
7. Collins CM, Liu W, Swift BJ, Smith MB. Combination of optimized transmit arrays and some receive array reconstruction methods can yield homogeneous images at very high frequencies. *Magn Reson Med* 2005;54(6):1327-1332.
8. Brunner DO, Pruessmann KP. B1(+) interferometry for the calibration of RF transmitter arrays. *Magn Reson Med* 2009;61(6):1480-1488.
9. Tse DH, Poole MS, Magill AW, Felder J, Brenner D, Jon Shah N. Encoding methods for B1(+) mapping in parallel transmit systems at ultra high field. *Journal of magnetic resonance* 2014;245:125-132.
10. Eichfelder G, Gebhardt M. Local specific absorption rate control for parallel transmission by virtual observation points. *Magn Reson Med* 2011;66(5):1468-1476.
11. Nehrke K, Bornert P. Eigenmode analysis of transmit coil array for tailored B1 mapping. *Magn Reson Med* 2010;63(3):754-764.
12. Hoffmann J, Budde J, Shajan G, Pohmann R. Slice-Selective B1 Phase Shimming at 9.4 Tesla. *Proc Intl Soc Magn Reson Med* 2010;18:2470.
13. Felder J, Hong S, Celik A, Park J, Geschewski F, Jeong H, Besançon E, Woo M, Brenner D, Cho Z, Shah N. RF Coil Array for Accelerated Excitation in Three Dimensions. *Proc Intl Soc Magn Reson Med* 2012;20:2609.
14. Hetherington HP, Avdievich NI, Kuznetsov AM, Pan JW. RF shimming for spectroscopic localization in the human brain at 7 T. *Magn Reson Med* 2010;63(1):9-19.
15. Van den Berg CA, van den Bergen B, Van de Kamer JB, Raaymakers BW, Kroeze H, Bartels LW, Legendijk JJ. Simultaneous B1 + homogenization and specific absorption rate hotspot suppression using a magnetic resonance phased array transmit coil. *Magn Reson Med* 2007;57(3):577-586.
16. Hou Z. A Review on MR Image Intensity Inhomogeneity Correction. *International Journal of Biomedical Imaging* 2006;2006.
17. Tustison NJ, Avants BB, Cook PA, Zheng YJ, Egan A, Yushkevich PA, Gee JC. N4ITK: Improved N3 Bias Correction. *Ieee T Med Imaging* 2010;29(6):1310-1320.
18. Christ A, Kainz W, Hahn EG, Honegger K, Zefferer M, Neufeld E, Rascher W, Janka R, Bautz W, Chen J, Kiefer B, Schmitt P, Hollenbach HP, Shen J, Oberle M, Szczerba D, Kam A, Guag JW, Kuster N. The Virtual Family--development of surface-based anatomical models of two adults and two children for dosimetric simulations. *Physics in medicine and biology* 2010;55(2):N23-38.
19. Nehrke K, Bornert P. DREAM--a novel approach for robust, ultrafast, multislice B(1) mapping. *Magn Reson Med* 2012;68(5):1517-1526.
20. Adriany G, Gozubuyuk A, Auerbach E, van De Moortele PF, Andersen P, Vaughan JT, Ugurbil K. A 32 channel Transmit/Receive Transmission Line Head Array for 3D RF Shimming *Proc Intl Soc Magn Reson Med* 2007;15:166.
21. Kozlov M, Turner R. Analysis of RF transmit performance for a 7T dual row multichannel MRI loop array. *Conference proceedings : Annual International Conference of the IEEE Engineering in Medicine and Biology Society IEEE Engineering in Medicine and Biology Society Annual Conference* 2011;2011:547-553.
22. Vaughan JT, Snyder CJ, DelaBarre LJ, Bolan PJ, Tian J, Bolinger L, Adriany G, Andersen P, Strupp J, Ugurbil K. Whole-body imaging at 7T: preliminary results. *Magn Reson Med* 2009;61(1):244-248.